Int. J. Electrochem. Sci., 17 **(2022)** Article Number: 221153, doi: 10.20964/2022.11.55

International Journal of ELECTROCHEMICAL SCIENCE
www.electrochemsci.org

Studies of the Corrosion Behaviours of High-strength Alloy Steel in an Environment Containing Cl^- Using a Wire Beam Electrode (WBE) and EIS Techniques

Dan Wang[1,2], *Qingdong Zhong*[2,3]

[1] College of Advanced Vocational Technical, Shanghai University of Engineering Science, Shanghai, 200437, P. R. China;
[2] Shanghai Key Laboratory of Modern Metallurgy and Material Processing, Shanghai University, Shanghai, 200444, P. R. China;
[3] School of Vanadium and Titanium, Panzhihua University, Panzhihua, 617000, P. R. China)
*E-mail: 731787218@qq.com

Received: 9 August 2022 / *Accepted:* 25 September 2022 / *Published:* 10 October 2022

The corrosion behaviours of BR1500HS and Aermet100 high-strength alloy steel in an environment containing Cl^- were investigated by wire beam electrode (WBE) and electrochemical impedance spectroscopy (EIS) techniques, and the corrosion products were analysed by scanning electron microscopy (SEM) and X-ray photoelectron spectrometry (XPS). The results showed that the microstructure of BR1500HS was coarse ferrite and pearlite, while that of Aermet100 was fine lath martensite. The WBE of BR1500HS showed general corrosion with a large number of total anodes (NTA) and a low localized corrosion intensity index *(LCII)*. While the WBE of Aermet100 displayed severe localized corrosion in the first 24 hours with a small NTA and a high *LCII*, the localized corrosion was inhibited after the 24th hour. The EIS of BR1500HS revealed a single time constant of reactive corrosion, while the EIS of Aermet100 showed that there was a diffusion phenomenon, and rust layer capacitance and rust layer resistance occurred. The corrosion products of BR1500HS composed of Fe_2O_3, FeOOH, Fe^{2+} satellites, Fe and Fe^{3+} satellites were coarse, loose and porous, and the Fe^{2+} oxide with high compactness accounted for only 33% of the total oxide. The corrosion products of Aermet100 composed of FeOOH, Fe^{2+} and Fe^{2+} satellites were small, uniform and dense, and the Fe^{2+} oxide with high compactness accounted for 74% of the total oxide. Combining the improvement of Co^{2+}, Ni^{2+}, Cr^{3+} and Mo^{6+} in corrosion products, Aermet100 showed a stronger corrosion resistance in the environment containing Cl^-.

Keywords: high-strength alloy steel; corrosion behaviour; Cl^-; wire beam electrode; electrochemical impedance spectroscopy

1. INTRODUCTION

Currently, high-strength alloy steel is one of the most popular materials and is widely used in the aerospace, automotive and marine industries [1-3]. Both BR1500HS and Aermet100 are high-strength alloy steels with excellent mechanical properties. Most previous studies on BR1500HS and Aermet100 were focused on their mechanical properties [4-6], while the corrosion resistance of BR1500HS and Aermet100 is also important for application in a corrosive environment. There are few previous studies on the corrosion characteristics of BR1500HS. Previous studies on the corrosion characteristics of Aermet100 paid more attention to the embrittlement resistance and uniform corrosion [7-9]. Figueroa et al.[7] researched the hydrogen diffusivity of 300M and Aermet100 and found that the reverted austenite forming around martensite laths during tempering enhanced the embrittlement resistance of Aermet100. Hu et al. [8] reported that there was a critical pH for Aermet100; Aermet100 steel exhibited an active dissolution state below the critical pH, while the steel would be passivated beyond the critical pH, and pits would be initiated by adding Cl^- into an acidic solution. Sun et al. [9] reported that the dense γ-Fe_2O_3 and Fe_3O_4 in the corrosion products of Aermet100 steel were the keys to hindering the diffusion of Cl^- and O_2 and improving the corrosion resistance when compared with 300M steel. The localized corrosion behaviour also had a great influence on the service life of BR1500HS and Aermet100 in corrosive environments, but there have been few studies on this topic.

The WBE technique is an important method to study localized corrosion behaviour. A single large-area metal electrode is divided into several small microelectrodes by the WBE so that the adjacent microelectrodes on the electrode surface can reflect the changes in electrochemical parameters in the microregion [10-11]. In previous studies, WBE has been widely used in evaluating the localized corrosion of organic coatings and the localized corrosion of the interface between metals and organic/inorganic phases [12-14]. Zhang et al. [12] discussed the corrosion initiation and development mechanism of steel under defective coatings in 3.5% NaCl solution by the WBE and EIS techniques. Tang et al. [13] reported that the WBE technique could effectively reflect the local electrochemical signal of a Ni-P coating in a 3.5 wt.% sodium chloride solution. The WBE and EIS techniques were also used by Liu et al. [14-15] to study the corrosion behaviour of a carbon steel/copper-nickel alloy couple under epoxy coating with an artificial defect in 3.5 wt.% NaCl solution. In addition, Parvizi et al. [16] researched the complex localized corrosion initiation and propagation processes of aluminium alloy AA2024-T3 by WBE with electrode wire diameters of 100 μm and 1 mm. Pang et al. [17] studied the localized corrosion of carbon steel by the in situ local damage of porous corrosion products using WBE technology.

In this paper, the corrosion behaviours of BR1500HS and Aermet100 high-strength alloy steel in an environment containing Cl^- were investigated by the WBE and EIS techniques, and the distribution of the real-time corrosion potential and corrosion current density of a BR1500HS WBE and an Aermet100 WBE were analysed statistically. The long-term variation in EIS plots was detected, and the corrosion products were studied to explain the reasons for the corrosion behaviours. The conclusions of this work will provide support for the application of high-strength alloy steel.

2. EXPERIMENTAL

2.1 Materials and sample preparation

Table 1. The chemical composition of BR1500HS (wt. %)

Sample	C	Si	Mn	Cr	Ti	S	P	Fe
BR1500HS	0.232	0.227	1.03	0.133	0.032	0.001	0.010	Bal.

Table 2. The chemical composition of Aermet100 (wt. %)

Sample	C	Cr	Co	Ni	Mo	Fe
Aermet100	0.23	3.05	12.85	11.06	1.14	Bal.

In this work, the wire beam electrodes (WBE) and single electrodes are made of BR1500HS and Aermet100, as listed in Table 1 and Table 2. The yield strength of BR1500HS is 1200 MPa, while that of Aermet100 is 1730 MPa. The WBE was made from 100 wires, and the diameter of the wire was 1 mm. The 100 wires were arranged in 10 × 10 after welding to 100 electrical wires while keeping a 1 mm distance between the wires by a mould, and then the wires were fixed with epoxy resin. The total testing area of the WBE was 0.785 cm^2. The single electrode with a testing area of 1 cm^2 was fixed with epoxy resin after welding to copper wires. The working surfaces of the electrodes were ground with silicon abrasive papers from 400# to 1000#, followed by cleaning with deionized water and anhydrous ethanol. A 3.5% NaCl solution was used to simulate the marine environment.

2.2 Morphology observation

The metallographic morphology and microstructure of BR1500HS and Aermet100 were observed by optical microscopy (OM, Olympus BC51M, Japan) and scanning electron microscopy (SEM, ZEISS Gemini SEM 300, Germany). The samples used to observe the microstructure were mechanically polished by a 0.25 μm diamond agent after grounding with silicon abrasive papers from 400# to 2000# and then etched with a 10% (in volume) nitrate alcohol solution.

2.3 Electrochemical tests

The WBE tests were accomplished by a WBE potentiometric current scanner (CST520, China), and a schematic diagram of the testing device is shown in Fig. 1. A saturated calomel electrode (SCE) was used as the reference electrode, a WBE was used as the working electrode, and the sampling frequency was 1 Hz. The scanner was equipped with a high-resolution potential tracker and an automatic zero-resistance galvanometer, which successfully obtained the open circuit potential between a single wire and the reference electrode and the coupling current between the tested wire and 99 other wires. There were 100 sets of low-power relays in the scanner to scan and detect the cyclic

potential/current density of 100 electrodes automatically, and the switching of different electrode current ranges was realized by the built-in electronic switch [17]. The real-time corrosion potential and current density were measured after 0.5 h, 8 h, 16 h, 24 h, 48 h, 96 h and 120 h of preimmersion. In addition to the WBE scanning, the wire terminals of the WBE electrode were connected to realize the movement of electrons freely.

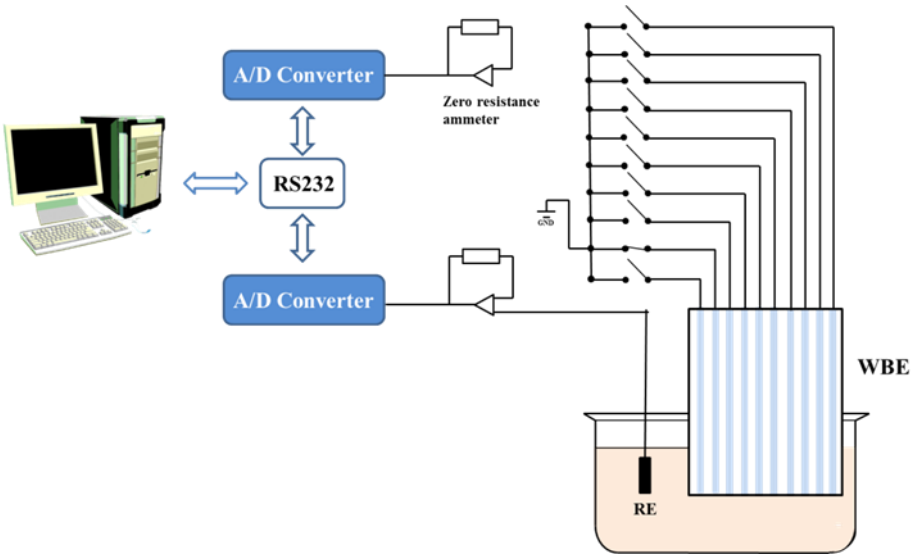

Figure 1. Schematic diagram of the WBE testing device

Electrochemical impedance spectroscopy (EIS) tests were performed with a three-electrode cell system using an electrochemical workstation (CS350, China). A single electrode was used as the working electrode, a platinum wire was used as the counter electrode, and a saturated calomel electrode (SCE) was used as the reference electrode. The frequency used in EIS tests ranged from 100 kHz to 10 mHz, and the signal used in EIS tests was a 5 mV amplitude AC signal. The EIS tests were performed at 0.5 h, 8 h, 16 h, 24 h, 48 h, 96 h, and 120 h of preimmersion to monitor the formation of the corrosion products.

2.4 Corrosion product analysis

The morphologies of the corrosion products were observed by scanning electron microscopy (SEM, HITACHISU-1510, Japan). X-ray photoelectron spectrometry (XPS, Thermo Scientific K-Alpha+, America)) was applied to the samples after 120 hours of immersion to analyse the composition of the corrosion products. XPS was carried out by using monochromatic AlKα radiation at 1486.6 eV, and the analysis chamber had a vacuum of 5×10^{-9} Mbar and a pass energy of 50 eV.

3. RESULTS AND DISCUSSION

3.1 Microstructural characteristics of BR1500HS and Aermet100

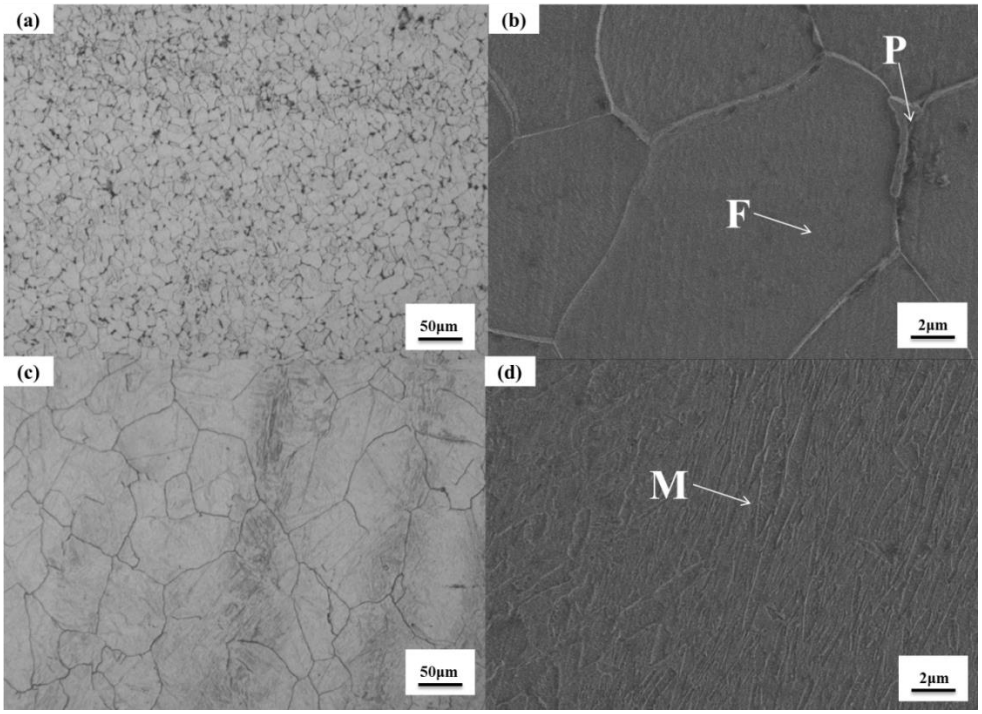

Figure 2. OM and SEM morphologies of BR1500HS and Aermet100: BR1500HS ((a) and (b)), Aermet100 ((c) and (d))

The metallographic morphology and microstructure of BR1500HS and Aermet100 are shown in Figure 2. Compared with Fig. 2(a) and (c), grains of BR1500HS were fine and homogeneous, while grains of Aermet100 were coarse. Fig. 2(b) and (d) show that the microstructure of BR1500HS was ferrite and pearlite, while that of Aermet100 was uniform and dense lath martensite. The difference in grain size and microstructure would affect the corrosion resistance of BR1500HS and Aermet100. The fine grains of BR1500HS would form a large number of grain boundaries, and the large number of grain boundaries provided a fast channel for the corrosion ions, for example, Cl^- [18], leading to the worse corrosion resistance of BR1500HS. In addition, the uniform and dense lath martensite was beneficial to improving the corrosion resistance of Aermet100 for fewer organizational defects.

3.2 Electrochemical behaviours

3.2.1 Current density distribution of the WBE

To research the localized corrosion behaviours of BR1500HS and Aermet100, the WBE technique was applied to reflect the real-time corrosion distribution.

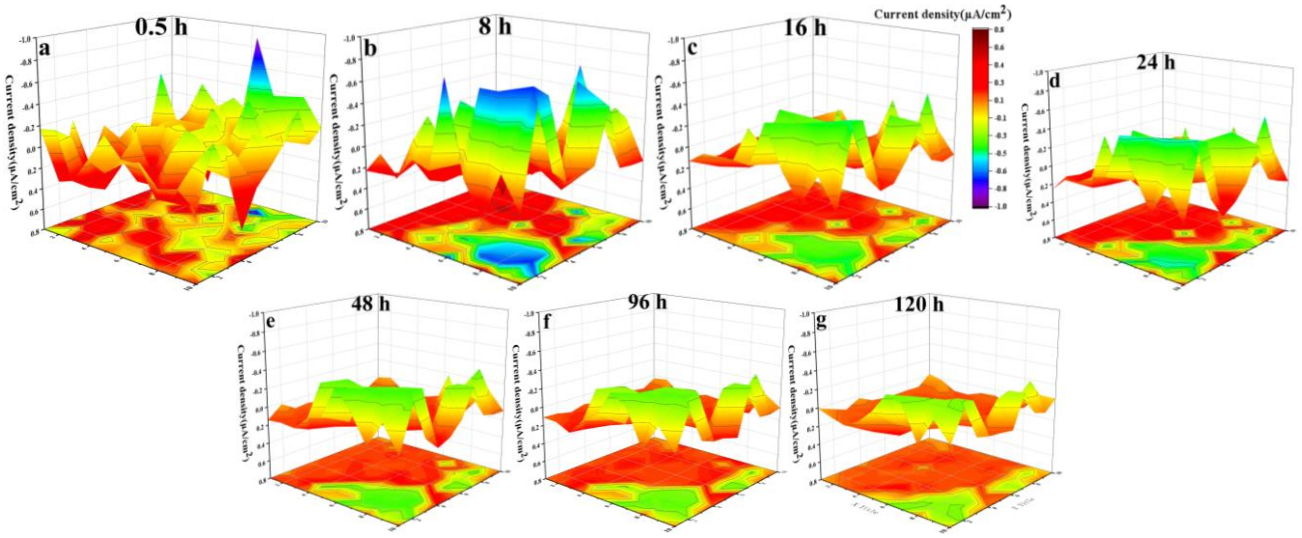

Figure 3. Current density distribution maps of the BR1500HS WBE in 3.5% NaCl solution at various immersion times: (a) 0.5 h; (b) 8 h; (c) 16 h; (d) 24 h; (e) 48 h; (f) 96 h; and (g) 120 h.

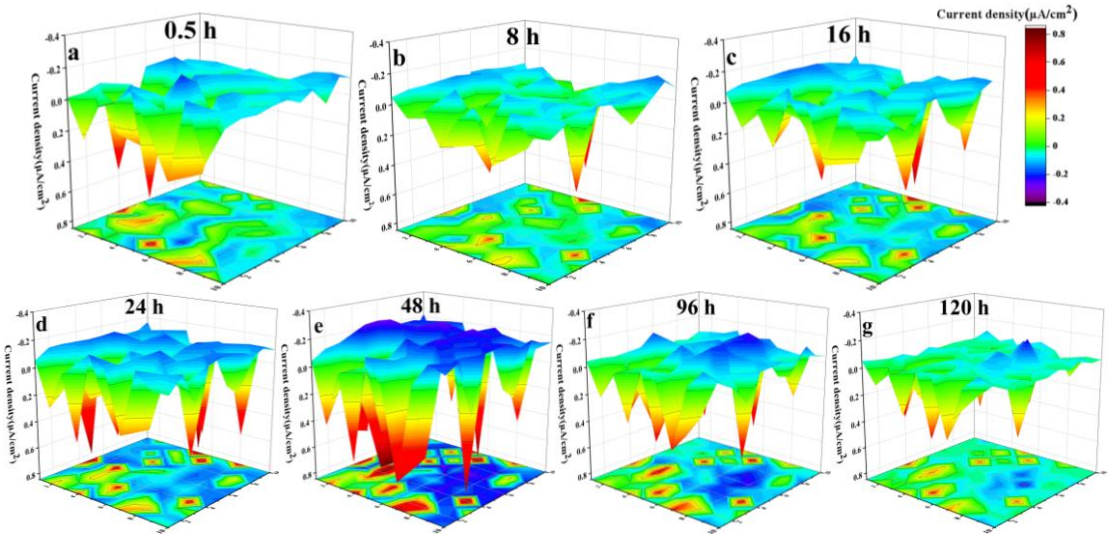

Figure 4. Current density distribution maps of the Aermet100 WBE in 3.5% NaCl solution at various immersion times: (a) 0.5 h; (b) 8 h; (c) 16 h; (d) 24 h; (e) 48 h; (f) 96 h; and (g) 120 h.

The variation in the current density distribution maps of the BR1500HS WBE in 3.5% NaCl solution is shown in Fig. 3. The cathodic current density was recorded as the negative value, while the anodic current density was defined as the positive value. The positions with cathodic current density were almost the same as the area of the anodic current density at the 0.5th hour. The current density distribution map displayed a structure of a "cathode-anode-cathode ring" [19], and the anodic areas revealed a serious corrosion reaction with a total anodic current density (I_a(total)) of 10 μA/cm^2. With prolonged soaking time, the positions with anodic current density expanded from the edge to the centre, and the anodic current density was enhanced with a more severe corrosion reaction of the anode at the 8th hour. From the 16th to the 120th hour, the anodic area accounted for almost 80% of the total

electrode, and the ratio tended to be stable so that the corrosion characteristics tended to be uniform corrosion.

Fig. 4 shows the current density distribution maps of the Aermet100 WBE in 3.5% NaCl solution at different immersion times. As shown in Fig. 4a, only a few anodes formed after immersion for 0.5 hours, and the anodic current density was small, which was probably due to the inhomogeneous distribution of metallurgical components [20]. More anodes formed, and the anodic current density increased after 8 hours, which suggested that the anodes of electrochemical reactions were enhanced, and the structure of the "small anode and large cathode" could promote the electrochemical reactions. The anodic current density increased unceasingly after the 8th hour, and the electrochemical reactions were the most serious at the 48th hour. From the 48th to the 120th hour, the anodic current density started to decrease, and the electrochemical reactions receded significantly due to the protective corrosion products on the anodes [21].

To more clearly identify the corrosion process of BR1500HS and Aermet100, the electrochemical parameters obtained from the current density distribution maps are shown in Fig. 5. In Fig. 5, I_a(max) represents the maximum anodic current density, I_a(total) represents the total anodic current density, I_c(max) represents the maximum cathodic current density, I_c(total) represents the total cathodic current density, NTA represents the number of total anodes, and NTC represents the number of total cathodes. According to Fig. 5(a), during the immersion of BR1500HS WBE in 3.5% NaCl solution, after 8 hours of exposure, the I_a(total) rose from 10 μA/cm^2 to 14.8 μA/cm^2, and the I_a(max) increased from 0.52 μA/cm^2 to 0.66 μA/cm^2, reflecting that the total anodic activity was enhanced, and with the continuous decrease in the NTC, the NTA continued to rise. From the 8th to 16th hour, I_a(total) and I_a(max) began to decrease, but the NTA continued to increase, which was consistent with the variety of positions of anodic current density in Fig. 3. Both I_a(max), I_a(total) and the NTA tended to be stable after the 16th hour, and thus, the occurrence of uniform corrosion for BR1500HS was further clarified in Fig. 5(a). As shown in Fig. 5(b), compared with BR1500HS, the electrochemical parameters of Aermet100 displayed different trends. I_a(max) and I_a(total) increased abruptly from the 0.5th to 48th hour; moreover, the maximum values of I_a(max) and I_a(total) were 0.825 μA/cm^2 and 11.87 μA/cm^2 at the 48th hour, respectively, and then I_a(total) and I_a(max) dropped continuously from the 48th to the 120th hour. Finally, I_a(total) and Ia(max) at the 120th hour were 0.46 μA/cm^2 and 4.94 μA/cm^2, respectively, which were lower than those at the 0.5th hour. In addition, the NTA was obviously reduced from beginning to end. These results demonstrated that the corrosion reactions were initiated at certain points because of the inhomogeneous distribution of chemical components, and corrosion reactions were intensified first and then suppressed for the formation of protective corrosion products.

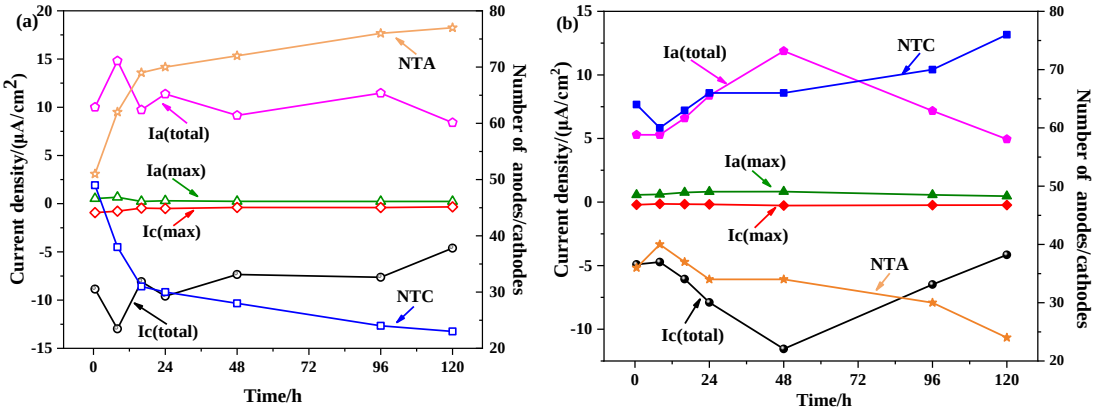

Figure 5. Trends of the parameters I_a(max), I_c(max), I_a(total), I_c(total), NTA and NTC gained from current density distribution maps with time: (a) BR1500HS, and (b) Aermet100

The localized corrosion intensity index (*LCII*) proposed by Tan et al. [10, 22] was calculated based on the electrochemical parameters in Fig. 5.

$$LCII = \frac{\mathrm{I}_a(\max)}{\sum 1_a^N I_a} \qquad (1)$$

where I_a is the anodic current density of the WBE. The *LCIIs* of BR1500HS and Aermet100 are presented as a function of time in Fig. 6. The *LCII* of BR1500HS was always lower than 0.1, while the *LCII* of Aermet100 was higher than 0.1 before the 24th hour and then lower than 0.1 after the 24th hour. According to Tan et al. [10, 22], when the *LCII* was not higher than 0.1, the localized corrosion was not serious. The corrosion type of BR1500HS was uniform corrosion, while the corrosion type of Aermet100 demonstrated that localized pitting was initiated before the 24th hour and that localized corrosion was inhibited after immersion for 24 hours in 3.5% NaCl solution.

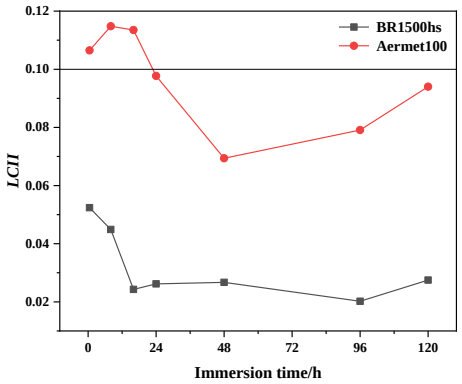

Figure 6. LCII of BR1500HS and Aermet100 soaked in 3.5 wt.% NaCl solution for 120 hours

3.2.2 EIS analysis

To further analyse the uniform corrosion of BR1500HS and Aermet100 in 3.5 wt.% NaCl solution, EIS was performed continuously during the immersion period, and the results are shown in Fig. 7 and Fig. 8. In Fig. 7(a), the Nyquist plots of BR1500HS show that the arc radius of the

capacitive reactance first decreased and then increased with time, and the minimum value of the arc radius of the capacitive appeared at the 16th hour. The corrosion reactions intensified gradually with time from the 0.5th to the 16th hour, and then the corrosion reactions were weakened from the 16th to the 120th hour. For the Bode plots of BR1500HS in Fig. 7(b), there was only one time constant in this reaction system, and the time constant continuously shifted towards low frequency during immersion, as the low medium frequency time constant was due to the electrochemically active surface [23]; thus, the electrochemical reaction had a tendency to intensify. Moreover, the maximum phase angle first decreased and then increased, which was consistent with the variation in the arc radius of the capacitive. These results demonstrated that severe corrosion occurred on the surface of BR1500HS from the 0.5th to the 16th hour with the corrosion products accumulating gradually, and the corrosion products could protect the matrix to some extent after the 16th hour, but the poor compactness of corrosion products resulted in its corrosion resistance being less than that of the matrix. As shown in Fig. 8(a), the Nyquist plots of Aermet100 showed that the arc radius of the capacitive reactance first decreased and then increased during the immersion period, and there was diffusion from the 16th to the 24th hour. In Fig. 8(b), the Bode plots of Aermet100 showed significant differences during the soaking period. In the beginning, there was only one time constant at the 0.5th hour, and the time constant turned to two at the 8th hour. Subsequently, the time constant was three from the 16th to 24th hour. Finally, the time constant was two again from the 48th to 120th hour. Usually, the time constant in low medium frequencies is due to an electrochemically active surface, while the time constant in high medium frequencies is associated with the rust layer capacitance and rust layer resistance on the electrode surface [24]. The high-frequency time constant of Aermet100 was attributed to corrosion product capacitance and resistance, while the medium-frequency time constant of Aermet100 was associated with diffusion from the 16th to the 24th hour. Therefore, the corrosion resistance of Aermet100 after the 16th hour was enhanced by the capacitance and resistance of the corrosion products. In addition, diffusion from the 16th to the 24th hour also had positive effects on the corrosion resistance.

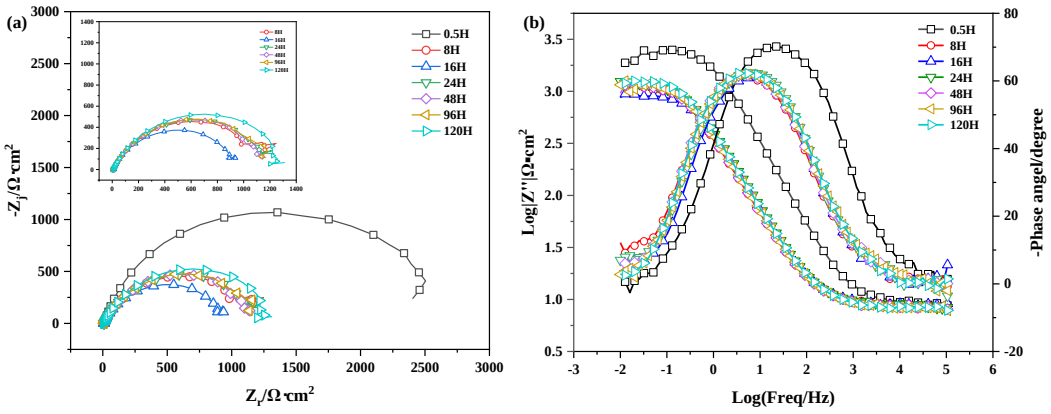

Figure 7. The electrochemical impedance spectroscopy variation of BR1500HS in 3.5% NaCl solution: (a) Nyquist plots and (b) Bode plots

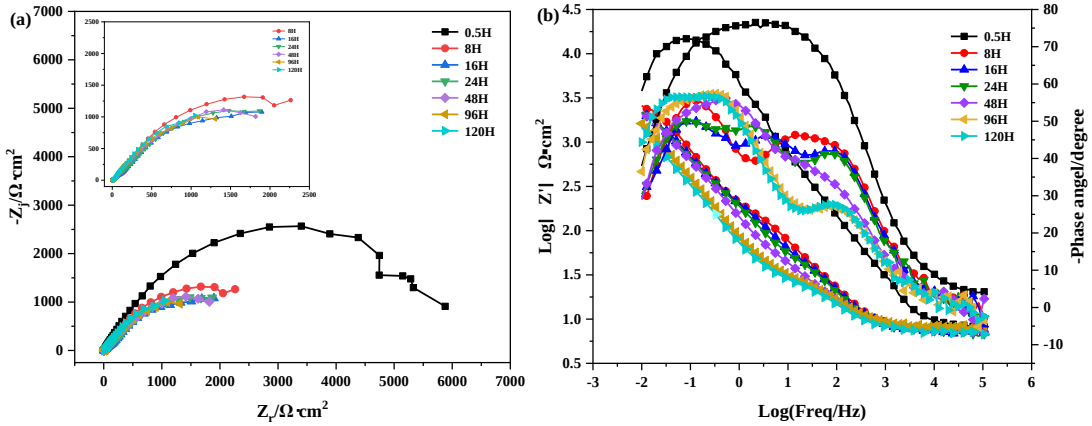

Figure 8. The electrochemical impedance spectroscopy variation of Aermet100 in 3.5 wt.% NaCl solution: (a) Nyquist plots and (b) Bode plots

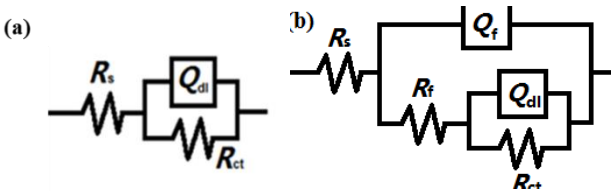

Figure 9. Equivalent circuits

Table 3. EIS parameters of BR1500HS and Aermet100 soaked in 3.5 wt.% NaCl solution for different times

Time(h)	BR1500HS		Aermet100		
	R_{ct}(Ω▪cm^2)	-Maximum phase Angle(°)	R_{ct}(Ω▪cm^2)	R_f(Ω▪cm^2)	-Maximum phase Angle(°)
0.5 h	2499	70.17°	4900	1857	76.50°
8 h	1250	61.40°	3490	270.2	55.46°
16 h	977.5	61.30°	4764	72.35	50.21°
24 h	1242	62.38°	5003	44.07	49.98°
48 h	1235	61.69°	3655	58.91	56.17°
96 h	1253	62.01°	3229	22.45	57.40°
120 h	1357	65.53°	3920	20.64	56.62°

The EIS data of BR1500HS could be fitted by the circuit in Fig. 9(a), while the circuit in Fig. 9(b) could be used to fit the impedance spectra of Aermet100 [25], where R_s represents the resistance of the solution, R_{ct} represents the resistance of charge transfer, Q_{dl} represents the capacitance of the double layer, R_f represents the resistance of corrosion products, and Q_f represents the capacitance of corrosion products. The electrochemical parameters for BR1500HS and Aermet100 are shown in Table 3. The R_{ct} of BR1500HS first decreased and then increased, which was consistent with the change in the arc radius of the capacitive reactance. While the R_{ct} of Aermet100 went through two cycles of

decreasing first and then increasing, these were consistent with the change in the arc radius and the existence and disappearance of diffusion in Fig. 8(a). Comparing the R_{ct} of BR1500HS and Aermet100, it could be found that the R_{ct} of Aermet100 was always greater than that of BR1500HS during immersion. For the R_f of Aermet100, the R_f was maximum at the 0.5th hour, which suggested that the passivation film existed on the surface of Aermet100 at that time. After immersion for 8 h, the R_f decreased rapidly, indicating that the passivation film was destroyed during immersion, and the R_f increased slightly after the 24th hour because of the accumulation of corrosion products replacing the passivation film to protect the matrix, but the protective effect of corrosion products was far lower than that of the original passivation film. In addition, the existence of corrosion products promoted an increase in R_{ct}, and both R_{ct} and R_f promoted an improvement in the corrosion resistance of Aermet100.

3.3 Corrosion resistance

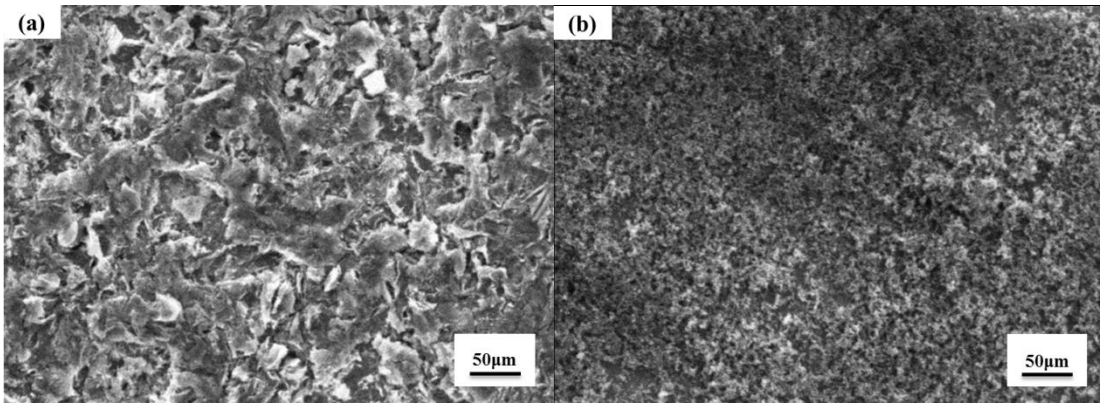

Figure 10. Morphologies of corrosion products soaked in 3.5 wt.% NaCl solution for 120 h: (a) BR1500HS and (b) Aermet100

The morphologies of the corrosion products of BR1500HS and Aermet100 immersed in 3.5 wt.% NaCl solution for 120 h are shown in Fig. 10. The corrosion products of BR1500HS were coarse, loose and porous, while the corrosion products of Aermet100 were fine, uniform and dense. The denser the corrosion products were, the higher the corrosion resistance, and thus, the corrosion resistance of Aermet100 was related to the morphology of the corrosion products.

XPS was employed to examine the corrosion products of BR1500HS and Aermet100 after immersion for 120 hours in a 3.5 wt.% NaCl solution. Fig. 11 shows the high-resolution Fe2p spectra of BR1500HS and Aermet100. After the background subtraction based on the Shirley algorithm [26], the Fe2p spectra of the corrosion products of BR1500HS were spilt into five peaks: Fe_2O_3 (710.8 eV), FeOOH (711.9 eV), Fe^{2+} satellite (714.3 eV), Fe (719.20 eV), and Fe^{3+}satellite (725.0 eV), while the Fe2p spectra of the corrosion products of Aermet100 were spilt into three peaks: FeOOH (711.9 eV), Fe^{2+} (715.8 eV), and Fe^{2+} satellite (723.4 eV), where Fe^{2+} (715.8 eV) mainly corresponded to divalent iron in Fe_3O_4. According to Fig. 11, it was obvious that the peaks of Fe^{3+} played a dominant role for

the corrosion products of BR1500HS, while the peaks of Fe^{2+} were predominant for the corrosion products of Aermet100.

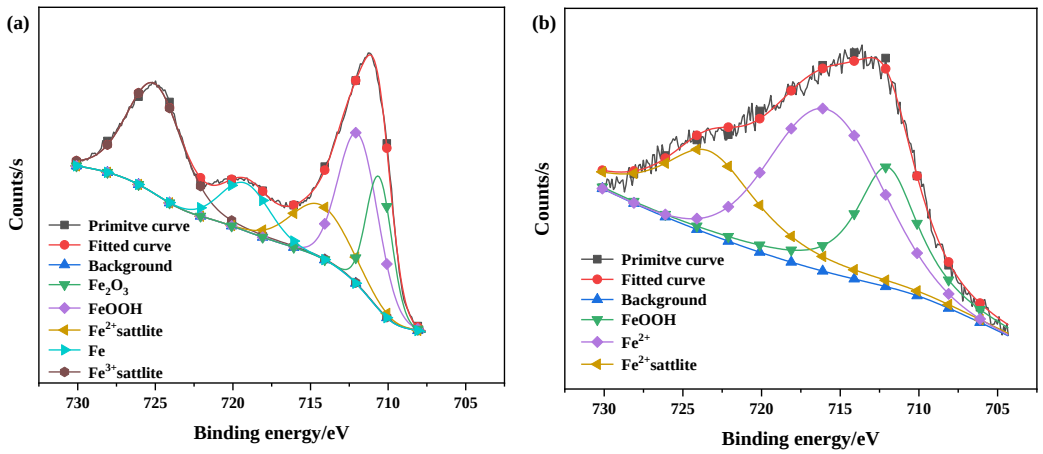

Figure 11. Typical Fe2p spectroscopy of corrosion products formed on samples after soaking in 3.5 wt.% NaCl solution for 120 h: (a) BR1500HS, (b) Aermet100

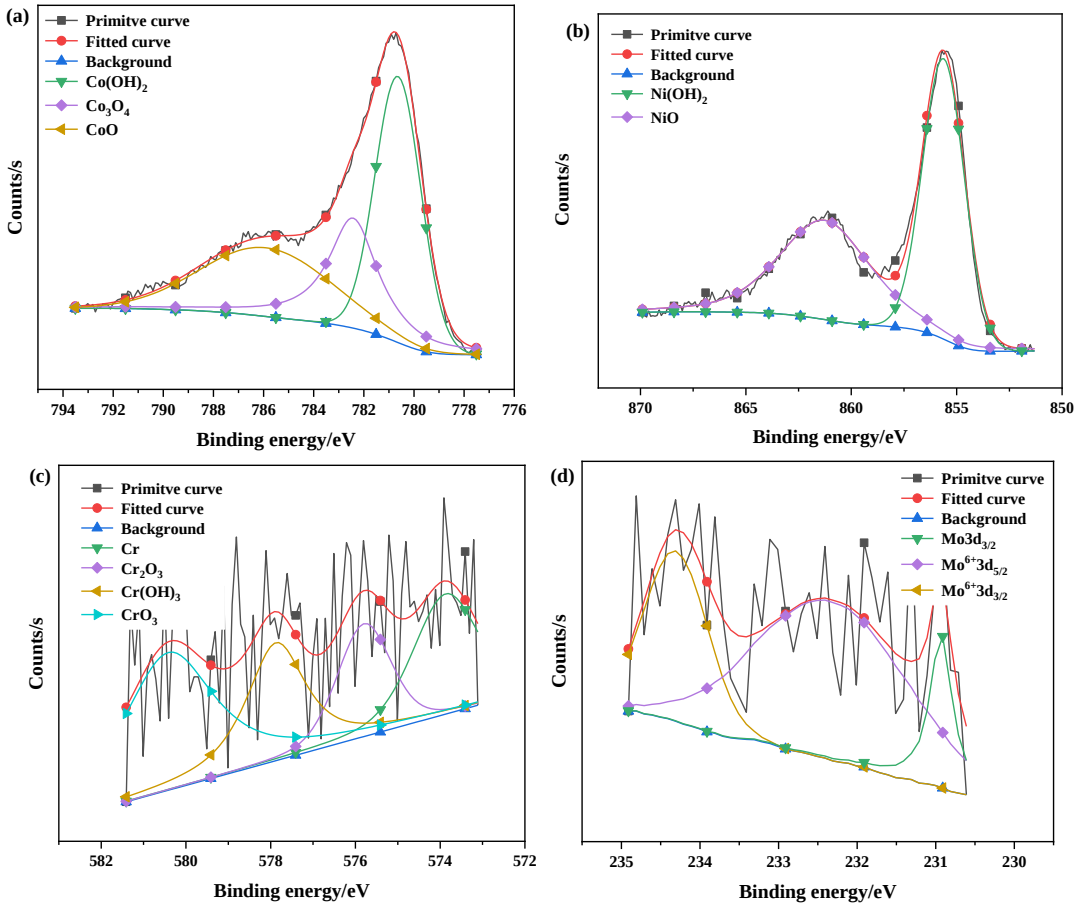

Figure 12. Typical spectroscopy of corrosion products formed on Aermet100 after soaking in 3.5 wt.% NaCl solution for 120 h: (a) Co2p, (b) Ni2p, (c) Cr2p, and (d) Mo3d

Based on the calculation of the peak area, the ratio of Fe^{2+}/Fe^{3+} for BR1500HS was 33%, while that for Aermet100 was 74%, as the densification of Fe^{2+} oxide in corrosion products is higher than that of Fe^{3+} oxide [27], and thus, the higher the ratio of Fe^{2+}/Fe^{3+} is, the denser the corrosion products, which coincided their morphologies.

Except for the analysis of iron oxides, other alloying elements in the corrosion products of Aermet100 after soaking for 120 hours in 3.5% NaCl solution were analysed by XPS, as shown in Fig. 12. As shown in Fig. 12(a), the Co2p spectrum was split into $Co(OH)_2$ (780.6 eV), Co_3O_4 (782.4 eV), and CoO (785.9 eV). The decomposition of the Ni2p spectrum revealed that there were two constituents representing $Ni(OH)_2$ (855.6 eV) and NiO (861.2 eV) in Fig. 12(b), both of which were Ni(II) compounds that could improve the ratio of Fe^{2+}/Fe^{3+} in corrosion products [28]. The Cr2p spectrum could be fitted with four peaks: Cr (573.9 eV), Cr_2O_3 (575.7 eV), $Cr(OH)_3$ (577.8 eV) and CrO_3 (580.4 eV) in Fig. 12(c), and the Cr^{3+} compounds account for 48% of the total Cr compounds, as Cr^{3+} could improve the self-repair and stability of the protective film [29]. Thus, Cr^{3+} could effectively promote the densification of corrosion products. The decomposition of Mo3d spectra showed a peak at 230.9 eV, which was attributed to molybdenum metal, a peak at 232.3 eV corresponding to $Mo^{6+}3d_{5/2}$, and a peak at 234.3 eV corresponding to $Mo^{6+}3d_{3/2}$ in Fig. 12(d), in which Mo^{6+} mainly consisted of $Fe_2(MoO_4)_3$ or MoO_3, and the corrosion products with Mo^{6+} could inhibit pitting of Aermet100 [30]. In addition, Ni and Mo were beneficial for enhancing the stability of Co compounds [31]. Therefore, the compounds formed by Co, Ni, Cr, and Mo and the Fe^{2+} compounds promoted the densification of corrosion products of Aermet100, retarding Cl^- ions from penetrating into the corrosion product film to improve its corrosion resistance.

4. CONCLUSIONS

(1) The grain size of BR1500HS steel was smaller than that of Aermet100, while the ferrite and pearlite of BR1500HS steel were much rougher than the fine martensite of Aermet100. The grain size of Aermet100 avoided the degradation of corrosion resistance caused by large grain boundaries, and the fine martensite of Aermet100 was beneficial for promoting corrosion resistance.

(2) According to the WBE tests, the NTA of BR1500HS increased rapidly and then tended to become stable, the *I*(total) increased first and then decreased to become stable, and the WBE of BR1500HS turned out to be generally corroded with a low *LCII*. The NTA of Aermet100 decreased continuously, but *I*(total) first increased and then decreased. The WBE of Aermet100 displayed severe localized corrosion in the first 24 hours with the high *LCII*, and the localized corrosion was inhibited after the 24^{th} hour. Based on the EIS tests, the reactance arc radius of BR1500HS and Aermet100 first decreased and then increased. The Bode plots of BR1500HS always revealed a single time constant of reactive corrosion, while the Bode plots of Aermet100 showed that the time constant of the diffusion phenomenon occurred in the medium frequency, and the time constant of the rust layer capacitance and rust layer resistance occurred in the high frequency.

(3) After soaking for 120 hours, both BR1500HS and Aermet100 were attached by corrosion products. The corrosion products of BR1500HS composed of Fe_2O_3, FeOOH, Fe^{2+} satellites, Fe and Fe^{3+} satellites were coarse, loose and porous, and the Fe^{2+} oxide with high compactness accounted for

only 33% of the total oxide. The corrosion products of Aermet100 composed of FeOOH, Fe^{2+} and Fe^{2+} satellites were small, uniform and dense, and the Fe^{2+} oxide with high compactness accounted for 74% of the total oxide. In addition, Co^{2+}, Ni^{2+}, Cr^{3+} and Mo^{6+} in the corrosion products of Aermet100 could improve the densification of corrosion products, and thus, dense corrosion products of Aermet100 enhanced the corrosion resistance.

References

1. J. Dong, C. Li and C. X. Liu, Y. Huang, L. M. Yu, H. J. Li and Y. C. Liu, *Mater. Sci. Eng. A*, 705 (2017) 249-256.
2. M. Morcillo, I. Díaz, B. Chico, H. Cano and D. Fuente, *Corros. Sci.*, 83 (2014) 6-31.
3. R. Nevshupa, I. Martinez, S. Ramos and A. Arredondo, *Mar. Struct.*, 60 (2018) 226-240.
4. B. L. Zhuang, Z. D. Shan, C. Jiang and X. Y. Li, *J. Iron. Steel. Res. Int*, 21 (2014) 606-613
5. Y. F. Lu, G. L. Wang, M. B. Zhang, R. S. Li and H. A. Zhang, *Addit. Manuf.*, 56 (2022) 102885.
6. C. W. Yao, X. T. Pang, Q. F. Gong, Z. J. Wang and P. L. Nie. *Mater. Sci. Eng. A*, 840 (2022) 142951.
7. D. Figuero and M.J. Robinson, *Corros. Sci.* 52 (2010) 1593-1602.
8. Y. B. Hu, C. F. Dong, M. Sun, K. Xiao, P. Zhong and X. G. Li, *Corros. Sci.* 53 (2011) 4159-4165.
9. M. Sun, K. Xiao, C. F. Dong, X. G. Li, *Acta. Metall. Sin*, 47 (2011) 442-448.
10. Y. J. Tan, N. N. Aung and T Liu, *Corros. Sci.*, 63 (2012) 379-386.
11. Y. J. Ta, *Corros. Sci.*, 41(1998) 229-247.
12. W. Zhang, J. Wang, Y. N. Li and W. Wang, *Acta Phys. -Chim. Sin.*, 26 (2010) 2941-2950.
13. Y. R. Tang, Q. Y. Wang, R. Pei, Y. C. Xi, L. J. Dong, S L Bai and S. H. Wan, *RSC Adv.*, 9 (2019) 34214.
14. J. Liu, Z. H. Lu, L. W. Zhang, C. P. Li, R. Ding, X. D. Zhao, P. Q. Zhang, B. Wang and H. T. Cui, *Prog. Org. Coat*., 148 (2020) 105909.
15. J. Liu, L. W. Zhang, X. L. Mu and P. Q. Zhang, *Prog. Org. Coat*., 111 (2017) 315-321.
16. R. Parvizi, A. E. Hughes and M. Y. J. Tan, *Corros. Sci.* 181 (2021) 109238.
17. L. Pang, Z. B. Wang, Y. G. Zheng, X. M. Lai and X. Han, *J. Mater. Sci. Technol.*, 54 (2020) 95-104.
18. Z. Q. Cao, W. H. Liu, R. Xue and Z. G. Zheng, *Chinese Journal of Rare Metals*, 30 (2006) 735-739.
19. B. Zhao, Y. X. Yu, J. Guo, T. Y. Zhou, S. W. Zou and T. Xu , *Materials & Corrosion Engineering Management*, 1 (2020) 27-30.
20. Y. J. Tan, *Hoboken, New Jersey : Wiley*, 2012.
21. A. Qian, P. Jin, X. M. Tan and D. Wang, *Surface Technology*, 2018, 47(10):231-239.
22. Y. J. Tan, N. N. Aung, *Mater. Corros.*, 65 (2014) 457-465.
23. L. Freire, M. J. Carmezim, M.G.S. Ferreira and M. F. Montemor, *Electrochim. Acta* 56 (2011) 5280-5289.
24. A. Bautista, G. Blanco, F. Velasco, A. Gutiérrez, L. Soriano, F. J. Palomares and H. Takenouti, *Corros. Sci.*, 51 (2009) 785-792.
25. Y. M. Fan, W. Liu, Z. T. Sun, Thee Chowwanonthapunya, Y. G. Zhao, B. J. Dong, T. Y. Zhang and W. Banthukul, *Constr. Build. Mater.*, 266 (2021) 120937.
26. D.A. Shirley, *Phys. Rev. B*, 5 (1972) 4709.
27. X. H. Sun, X. B. Zuo, G. J. Yin, K. Jiang and Y. J. Tang, *Constr. Build. Mater.*, 150 (2017) 703-713.
28. Y. W. Tian, C. F. Dong, G. Wang, X. Q. Cheng and X. G. Li, *Constr. Build. Mater.*, 246 (2020) 118462.
29. M. Liu, X. Q. Cheng, X. G. Li, Y. Pan and J. Li, *Appl. Surf. Sci.*, 389 (2016) 1182-1191.
30. J. Moon, H. Y. Ha , S. J. Park, T. H. Lee, J. H. Jang, C. H. Lee, H. N. Han and H. U. Hong, *J. Alloy.*

Compd., 775 (2019) 1136-1146.
31. E. Gomez, E. Pellicer, and E. Vallés, *Electrochem. Commun.*, 7 (2005) 275-281.